

Designing multifunctional cancer-targeted nanosystem for magnetic resonance molecular imaging-guided theranostics of lung cancer

Peng Gao^{a,b,*}, Chaoming Mei^{c,*}, Lizhen He^c, Zeyu Xiao^a, Leung Chan^c, Dong Zhang^a, Changzheng Shi^a, Tianfeng Chen^c and Liangping Luo^a

^aMedical Imaging Center, First Affiliated Hospital of Jinan University, Guangzhou, China; ^bDepartment of Radiology, Guangdong Women and Children Hospital and Health Institute, Guangzhou, China; ^cDepartment of Chemistry, Jinan University, Guangzhou, China

ABSTRACT

The integration of diagnosis and therapy is an effective way to improve therapeutic effects for cancer patients, which has acquired widely attentions from researchers. Herein, a multifunctional drug-loaded nanosystem (F/A-PLGA@DOX/SPIO) has been designed and synthesized to reduce the side effects of traditional chemotherapy drugs and realize simultaneous tumor diagnosis and treatment. The surface modification of folic acid (FA) and activatable cell-penetrating peptide (ACPP) endows the nanosystem with excellent cancer targeting capabilities, thus reducing toxicity to normal organs. Besides, the F/A-PLGA@DOX/SPIO nanosystem can serve as an excellent magnetic resonance imaging (MRI) T_2 -negative contrast agent. More importantly, according to *in vitro* experiments, the F/A-PLGA@DOX/SPIO nanosystem can promote the overproduction of reactive oxygen species (ROS) within A549 lung cancer cells, inducing cell apoptosis, greatly enhancing the antineoplastic effect. Furthermore, with the help of MRI technology, the targeting imaging of the F/A-PLGA@DOX/SPIO nanosystem within tumors and the dynamic monitoring of medicine efficacy can be realized. Therefore, this study provided a multifunctional drug-loaded F/A-PLGA@DOX/SPIO targeted nanosystem for magnetic resonance molecular imaging-guided theranostics, which has excellent potential for the application in tumor diagnosis and therapy.

ARTICLE HISTORY

Received 13 May 2018
Revised 24 June 2018
Accepted 25 June 2018

KEYWORDS

magnetic resonance imaging (MRI); molecular imaging (MI); superparamagnetic iron oxide (SPIO); theranostics; tumor targeting;






1. Introduction

Currently, chemotherapy remains the main treatment method for patients with advanced tumors who are unable to receive operative treatments (Rossi et al., 2014). Unfortunately, traditional chemotherapy drugs tend to trigger tumor multidrug resistance (MDR) and then lead to chemotherapy failure (Fang et al., 2012). In addition, chemotherapy drugs, which are nonselective, are usually toxic and have negative side effects on normal organs, restricting clinical applications to some extent. Currently, several approaches including physical targeting, proactive targeting, and reactive targeting have been applied to solve chemotherapy drugs in clinical problems. Among them, proactive target is based on the interaction of special receptors which expressed in cancer cells and targeting peptides, such as folic acid (FA), arginine-glycine-aspartic acid (RGD), and biotin, which has attracted more and more attention.


Besides, the emergence and development of nanotechnology provided novel vitality for the treatment of cancer in recent years, due to its advantages of easy targeting modification, long circulation, and retention time and wide

applications in the field of targeted therapy, molecular diagnosis, and tumor imaging. Meanwhile, a new multifunctional drug-loaded targeted nanosystem, which integrates drugs and contrast agents into nanoparticles (NPs), can not only serve as an excellent imaging cooperatively under lower drug dosages, but also show strong anticancer activities. Thus, it reduces toxicity to normal organs and could be very promising. This will, with the imaging probe of the nanoplat-form, realize efficient and targeted drug transfer, reduce drug side effects, and overcome tumor MDR (Chen et al., 2011; Nazir et al., 2014), enabling traditional chemotherapy drugs to have new possibilities.

Based on traditional imaging, molecular imaging (MI) employs specific molecular probes to realize the optimal dosage regimen and personalized treatment monitoring for tumors (Veeravagu et al., 2008). A molecular probe is an imaging agent (Rajendran & Mankoff, 2007) that can detect and describe the biological process of an *in vivo* system and present molecule information via medical imaging equipment. At present, superparamagnetic iron oxide (SPIO) is frequently used as a magnetic resonance imaging (MRI) T_2 -negative contrast agent. With excellent superparamagnetic

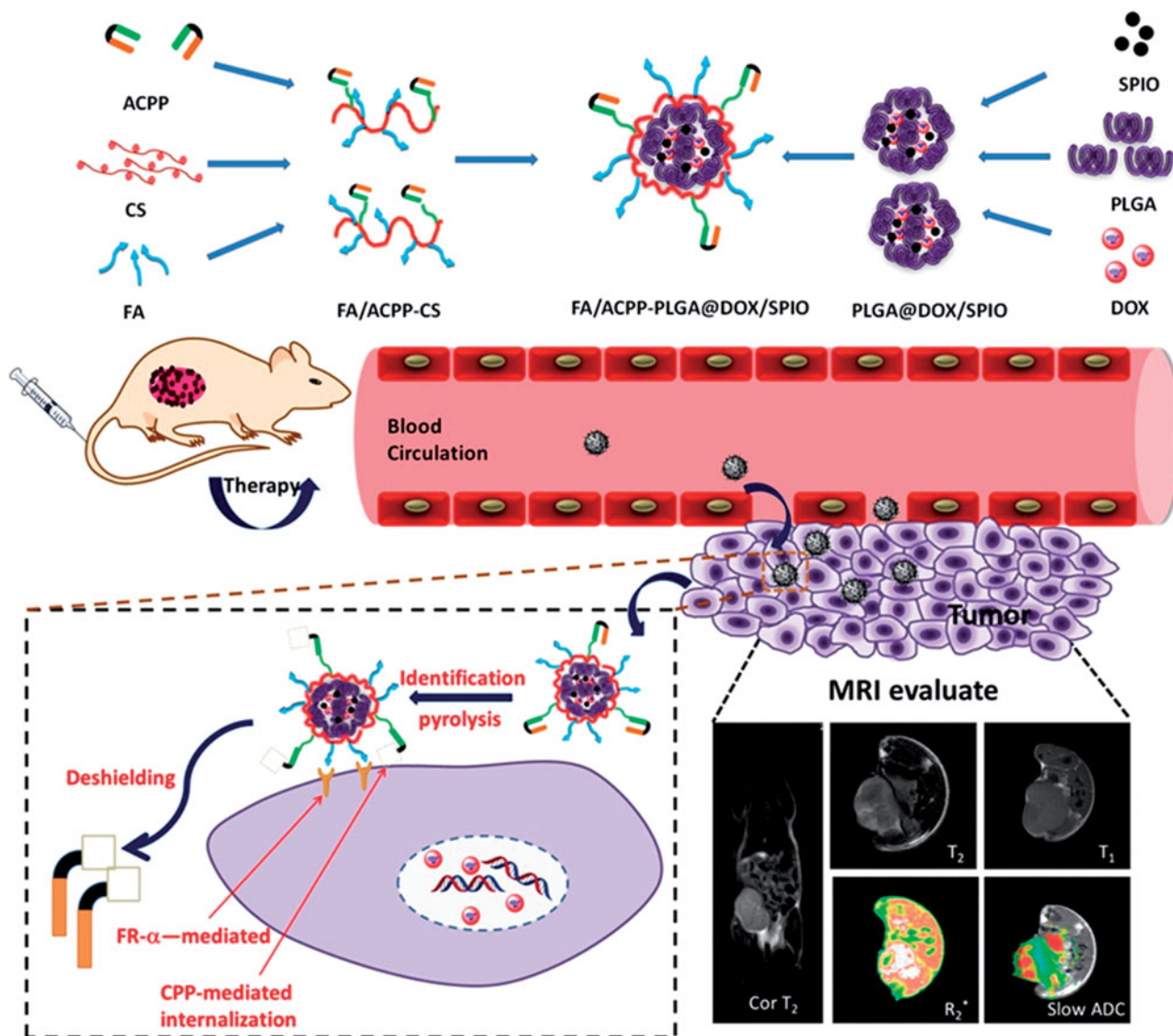
CONTACT Changzheng Shi  sczcn@126.com; Liangping Luo  tluolp@jnu.edu.cn  Medical Imaging Center, First Affiliated Hospital of Jinan University, Guangzhou 510630, China; Tianfeng Chen  tchentf@jnu.edu.cn  Department of Chemistry, Jinan University, Guangzhou 510632, China

*Both of these authors are first coauthors.

 Supplemental data for this article can be accessed [here](#).

© 2018 The Author(s). Published by Informa UK Limited, trading as Taylor & Francis Group.

This article is distributed under the terms of the Creative Commons Attribution-NonCommercial 4.0 License (<http://www.creativecommons.org/licenses/by-nc/4.0/>) which permits non-commercial use, reproduction and distribution of the work without further permission provided the original work is attributed as specified on the SAGE and Open Access pages (<https://us.sagepub.com/en-us/nam/open-access-at-sage>).



Scheme 1. Schematic illustration of the rational design of F/A-PLGA@DOX/SPIO nanoparticles for tumor magnetic resonance imaging and curative effect detection *in vivo*.

performance, SPIO is mainly employed to shorten T_2 relaxation time and weaken the T_2 -weighted signal. This type of contrast agent has a small particle size, strong penetrability, and a relaxation rate that is 7–10 times greater than that of Gd^{3+} under equal conditions. According to relevant experimental results, cells marked by SPIO have no short-term or long-term side effects, which is a safe and efficient molecule probe with high specificity, now widely used in the field of MR molecule imaging research (Sherry & Woods, 2008; Kim et al., 2010; Jafari et al., 2015). The SPIO has been approved by the Pure Food and Drug Administration (FDA) to be used in clinical practice (McBain et al., 2008) to dynamically monitor the image diagnosis of tumors *in vivo* and the targeted tumor treatment field (Chu et al., 2013; Majd et al., 2013) by acting as a carrier for chemotherapy drugs. Therefore, with the realization of longer blood half-life, SPIO, as a contrast agent, can be used for the imaging of tumor cells and molecule levels, improving the sensitivity of MRI techniques.

Currently, there have been research and reports on multifunctional drug-loaded nanosystem designed for tumor

treatment and imaging. For example, Yang et al. (2011) have developed SPIO NPs that allow the realization of PET/MRI tumor dual-mode tomography. The multifunctional NPs developed by Wang et al. (2013) were carried by mesoporous silica and modified by FA on the surface, which showed a higher drug absorption rate by the tumor. FA-conjugated SPIO NPs developed by Li et al. (2016a), which served as an MRI contrast in tumor-targeting MR imaging. Maeng et al. (2010) have reported a multifunctional drug delivery nanosystem (YCC-DOX) composed of poly(ethylene oxide)-trimellitic anhydride chloride-folate (PEO-TMA-FA), DOX, SPIO, and FA, which efficiently inhibited tumor growth without suffering any toxic effects and monitoring the progress of the cancer using MRI. However, there are few research reports on *in vivo* drug tractography via MRI and the dynamic evaluation of the drug-loaded nanosystem treatment effect.

Therefore, in this study, we focus on integrating tumor diagnosis and treatment using PLGA (poly(lactic-co-glycolic acid)) as a carrier, loading doxorubicin (DOX) and SPIO, and using FA and activatable cell-penetrating peptide (ACPP) as a

dual probe to modify and prepare the multifunctional drug-loaded nanosystem, FA/ACPP-CS-PLGA@DOX/SPIO (F/A-PLGA@DOX/SPIO). The design and synthesis protocol of the agent are shown in [Scheme 1](#). A series of bioactivity research was conducted on cell and protein levels by synthesizing a F/A-PLGA@DOX/SPIO nanosystem to discuss the effect and functioning mechanism of F/A-PLGA@DOX/SPIO on antineoplastic activity. Then, A549 xenografts in BALB/c nude mouse model were established to comprehensively evaluate the *in vivo* antineoplastic effect and safety of the F/A-PLGA@DOX/SPIO nanosystem. At the same time, MRI technology was used to trace and dynamically monitor the distribution of the F/A-PLGA@DOX/SPIO nanosystem within the tumor cells, realize targeted imaging and *in vivo* dynamic monitoring of the efficacy of tumor therapy, and study the antineoplastic functioning mechanism of the F/A-PLGA@DOX/SPIO nanosystem to provide a new theoretical foundation and iconography support for the integration of tumor diagnosis and treatment.

2. Materials and methods

2.1. Synthesis of F/A-PLGA@DOX/SPIO NPs

2.1.1. Activation of FA and ACPP

We dissolved 16 mg of FA in 0.8 mL (0.1 mol/L) of NaOH, added EDC (1-ethyl-3-[3-dimethylaminopropyl]carbodiimide hydrochloride) (250 μ L, 0.1 mol/L) and NHS (N-hydroxysuccinimide) (250 μ L, 0.1 mol/L) (EDC:NHS = 1:1) to the solution to react away from light for 2 h.

We dissolved 25 mg of ACPP in 1 mL pure water, added EDC (250 μ L, 0.1 mol/L) and NHS (250 μ L, 0.1 mol/L) (EDC:NHS = 1:1) to the solution to react away from light for 4 h.

2.1.2. Synthesis of CS-PLGA@DOX/SPIO

We weighed 5 mg of DOX, added a small amount of pure water, and fully mixed them with 1 mL (4 mg/mL) of SPIO (XFNANO Materials Tech, Nanjing, China.). We added 1 mL of PLGA (5 mg/mL) and 2 mL of acetone into the mixture and blended it overnight. After that, 1 mL of CS (6 mg/mL) was added to the above mixture and stirred for 6–8 hours.

2.1.3. Synthesis of F/A-PLGA@DOX/SPIO nanosystem

Activated FA and ACPP were added to the CS-PLGA@DOX/SPIO, stirring and react away from light for 24 h at room temperature to form the F/A-PLGA@DOX/SPIO nanosystem. After 24 h of dialysis to eliminate excess EDC and NHS, the samples were collected and stored at 4 °C in reserve.

2.2. Characterization

A high-resolution transmission electron microscope (HR-TEM, Hitachi H-7650, 80 kV) was used to characterize the appearance of F/A-PLGA@DOX/SPIO, and a Nano-ZS particle analyzer (Malvern Instruments Limited, Malvern, UK) was used to characterize stability, particle distribution, and zeta potential.

We used Fourier transform infrared spectroscopy (FT-IR, Equinox 55, Bruker, Billerica, MA, USA) to analyze and detect the coupled mode of the characteristic functional group after targeted modification of F/A-PLGA@DOX/SPIO. ¹H-NMR spectrum was used to analyze the chemical structure of F/A-PLGA@DOX/SPIO.

2.3. F/A-PLGA@DOX/SPIO in vitro T₂ relaxation performance

A GE 1.5 T clinical MRI system (Signa HDxt, Milwaukee, WI) was used to detect the MR radiography performance of F/A-PLGA@DOX/SPIO. We combined SPIO and F/A-PLGA@DOX/SPIO, commercialized contrast agents, with a nutrient solution to form solutions of different concentrations (0, 0.014, 0.028, 0.055, 0.11, and 0.22 mol), added the solutions in sequence into a 96-pore plate, and put them in a water tank. We selected an eight-channel wrist coil to conduct the T₂-weighted imaging (T₂WI). The horizontal relaxation rate (r^2) was obtained by plotting the relation curve of 1/T₂ value and Fe concentration.

2.4. Hemolysis assay

The SPIO (5 mg/L), DOX (5 mg/L), 0.5 mL of F/A-PLGA@DOX/SPIO (5 mg/L), and negative control (0.5 mL of normal saline) were each incubated with 0.5 mL of the red blood cell suspension for 1, 2, and 4 h. The hemolysis of the red blood cells exposed to SPIO, DOX, and F/A-PLGA@DOX/SPIO NPs was investigated by spectrophotometry (Nogueira et al., 2011). We used a fluorescent microscope (EVOS FL Auto, Life Technologies, Walsham, MA, USA) to observe the appearance of red blood cells after they were treated for 1, 2, and 4 h. In addition, we further detected the stability of F/A-PLGA@DOX/SPIO nanosystem in plasma using a Nano-ZS particle analyzer (Malvern Instruments Limited, Malvern, UK) (see the detailed experimental methods in the literature [Ma et al., 2018]).

2.5. Cell culture and in vitro cytotoxicity test

The cell lines involved in the experiments of this thesis were purchased from ACCT Company (ATCC, Manassas, VA) in USA; the human non-small cell lung cancer (NSCLC) cell is an A549 cell, and the normal liver cell is an L02 cell. All cells adopted in the experiments were cultivated under steady conditions (37 °C, 5%CO₂) in high-sugar culture media with fetal bovine serum (10%) and streptomycin–penicillin (1%). When the cells reached steady growth status, those in logarithmic phase were taken for *in vitro* activity tests. The cell viability (2×10^4 cells/mL) after treatment with different concentrations of DOX, FA-PLGA@DOX/SPIO, ACPP-PLGA@DOX/SPIO, and F/A-PLGA@DOX/SPIO for 72 h was determined using an MTT assay. To examine the relative cytotoxicity and the cell growth inhibitory effects of F/A-PLGA@DOX/SPIO NPs on different cells, we performed an MTT assay as previously described (Chen & Wong, 2009b). Further, we evaluated the safety of the nanosystem by the Safety Index (SI).

The SI was calculated and defined as the toxicity $IC_{50}/tumor\ IC_{50}$, where toxicity IC_{50} is defined as the concentration of nanosystem that kills 50% of the normal cell line and tumor IC_{50} is the concentration that kills 50% of cancer cell.

2.6. Cellular uptake and intracellular trafficking of NPs

A549 and L02 cells were inoculated at the density of 10×10^4 cells/mL into a 96-pore plate to be cultivated overnight. 0.5 mg/mL of DOX and F/A-PLGA@DOX/SPIO were added to the incubator for different durations; culture media were collected at 0, 0.5, 1, 2, 4, and 6 h, and a mixture of 100 μ L HCl-DMSO (1:4) was added to dissolve cells. Then, F/A-PLGA@DOX/SPIO and DOX solutions in the same block were diluted to equal ratios according to their concentrations. The light absorption of each pore was detected via fluorescence microplate (Spectra Max M5, BioTek, Winooski, VT). The amount of DOX and F/A-PLGA@DOX/SPIO absorbed by the cells was calculated at different times through the standard curve.

A Lyso-tracker was employed to track the position of F/A-PLGA@DOX/SPIO in the A549 cells. First, A549 cells were cultivated at a density of 5×10^4 cells/mL in the 2-cm-thick culture medium. After 24 h, F/A-PLGA@DOX/SPIO of a certain concentration was added, incubated for 8 h, and disposed at 0, 1, 2, 4, 6, and 8 h. Later, the green lysosomal marker, Lyso-tracker (1 μ g/ml), and nucleus blue marker, Hoechst 33342 (0.1 μ g/mL), were used to incubate cells for 1.5 h and 30 min, respectively. Finally, we collected fluorescence cell images using a fluorescence microscope (EVOS FL Auto, Life Technologies, 20 \times ,Walsham, MA, USA).

2.7. Drug-releasing evaluation of NPs

We measured three 0.5-mL portions of F/A-PLGA@DOX/SPIO in test tubes and added PBS (pH = 7.4), PBS (pH = 5.3), and A549 cell lysis buffer into the tubes. We incubated them at 37 $^{\circ}$ C away from light, collected 100 μ L suspensions at 0, 1, 3, 6, 12, 24, 36, 48, 60, and 72 h, centrifuged them, and took the supernatant. After the experiment was finished, we used a multifunctional fluorescent enzyme meter (Cytation 5, BioTek) to detect the absorption of the mixture and calculated DOX release according to the standard curve equation. Then, we drew the release curve of the drug-loaded nanosystem.

2.8. In vitro magnetic resonance imaging of NPs

Referring to the commercialized SPIO, we combined the serum-free media with F/A-PLGA@DOX/SPIO sample concentrations (calculated by Fe content) of 0, 3.125, 6.25, 12.5, and 25 μ g/mL. The serum-free media were incubated with A549 cells for 2 h. We put the solution under a GE 1.5T clinical MR system (Signa HDxt, Milwaukee, WI) equipped with a human eight-channel wrist coil to conduct T_2 WI scanning. DOX and F/A-PLGA@DOX/SPIO of the same concentration (0.5 mg/mL) were incubated with the A549 cells and underwent T_2 WI scanning for 0, 1, 2, and 4 h.

2.9. Flow cytometric analysis of cell cycle distribution

We analyzed the changes of A549 cell cycle and apoptosis ratio caused by F/A-PLGA@DOX/SPIO. We used Multicycle (Phoenix Flow Systems, San Diego, CA) software to analyze cell cycle distribution and hypodiploid peak to quantitate apoptosis (see the detailed experimental methods in the literature [Fan et al., 2013]).

2.10. Determination of intracellular reactive oxygen species (ROS) generation

We adopted conventional approaches for the passage of A549 cells, and after 24 h of anchorage growth of A549 cells in culture media, we added 10 μ L of DHE probe (drug concentration was 10 μ M after dilution) and F/A-PLGA@DOX/SPIO and DOX at preset concentrations. The fluorescence absorption value of each pore was measured regularly over 2 h and, in the meantime, a fluorescence microscope (EVOS FL Auto, Life Technologies, Walsham, MA, USA) was used to monitor the fluorescence signal intensity of the cells. After the ratio of absorption between the two groups was calculated, we analyzed the ROS change within the cells under the impact of F/A-PLGA@DOX/SPIO and DOX (see the detailed experimental methods in the literature [Fan et al., 2013]).

2.11. Western blot analysis

The effects of related proteins associated with different signaling pathways on the expression levels were determined by Western blot analysis (Chen & Wong, 2009a).

2.12. Tumor model

Male BALB/c nude mice (3–4 weeks old, weighing 13–15 g) were purchased from Beijing HFK Bioscience. All animal experiments were authorized by the Ethical Committee of Jinan University. We used precooled PBS to dilute and adjust A549 cell density to 3×10^7 cells/mL and injected 0.2 mL cells per mouse into the right-rear leg of the BALB/c nude mice (4–5 weeks old). One week later, tumors were formed with a transverse diameter of 5–8 mm. We observed the tumor-forming process daily and recorded the body weight of the nude mice and the size of tumors.

2.13. In vivo MR R_2^* imaging

When the diameter of the A549 subcutaneously implanted tumor was approximately 8–10 mm, we selected 12 tumor-bearing mice and dividing them into three groups with four in each group. Each group experienced MR base scanning before drug delivery. A group was injected with either SPIO (5 mg/kg), F/A-PLGA@SPIO (5 mg/kg), or F/A-PLGA@DOX/SPIO (5 mg/kg), all by means of caudal vein drug delivery. We used a GE 1.5T clinical MR system (Signa HDxt, Milwaukee, WI) and animal-specific mouse coils to conduct T_2 WI and R_2^* scanning over three consecutive days on the subcutaneously

implanted tumors of the 12 nude mice. Checking points were the base before the drug and 1, 4, 12, 24, 48, and 72 h after the drug.

2.14. In vivo assessment of therapy effect

When the volume of the A549 subcutaneously implanted tumor was approximately 100 mm^3 (with the short diameter being 4–6 mm and the long diameter being 6–8 mm), we selected 32 tumor-bearing mice and divided them into four groups. Group 1 was injected with normal saline as a control, Group 2 was injected with DOX at a concentration of 2 mg/kg, Group 3 was injected with F/A-PLGA@DOX/SPIO at a concentration of 1 mg/kg (low dose), and Group 4 was injected with F/A-PLGA@DOX/SPIO at a concentration of 2 mg/kg (high dose), all using the caudal vein drug delivery method.

The experimental nude mice were given drugs intravenously every two days for a total of 28 days and 14 doses. During the experiment, the body weight and tumor size of the mice were measured and recorded daily. Tumor volume change (%) was evaluated after the experiment and tumor growth-time and body weight-time curves of nude mice were drawn. Observation indicators included: (1) tumor volume = $ab^2/2$, (where a is the long diameter of the tumor and b is the short); (2) relative tumor volume (RTV) based on the measurement results, $RTV = V_t/V_0$ (where V_0 is the measured tumor volume of sub-caged drug delivery and V_t is the tumor volume at each measurement); (3) evaluation index of anti-tumor activity, relative tumor proliferation rate, T/C (%) = $TRTV/CRTV \times 100$ (where TRTV is the RTV of the treatment group and CRTV is the RTV of model contrast group); (4) evaluation index of anti-tumor activity, tumor growth inhibition rate (%) = $(\text{average tumor weight of model contrast group} - \text{average tumor weight of the treated group}) / \text{average tumor weight of model contrast group} \times 100$.

2.15. In vivo IVIM-DWI MRI

The experimental nude mice were routinely scanned by T_2WI and intra-voxel incoherent motion diffusion-weighted imaging (IVIM-DWI) over 28 days. Six-time points, the base before receiving the drug, the 3rd, 7th, 14th, 21st, and 28th day after receiving the drug, were taken.

2.16. Hematological and histological analysis

After MR R_2^* scanning, the 12 nude mice were executed and all their tumor tissue, heart, liver, spleen, kidneys, and lungs were removed, paraffin-embedded, sectioned, and Prussian blue stained. Twenty-eight days after the curative effect analysis, approximately 2 mL of blood was drawn from the live eye of the nude mice and about 500 μL of serum was obtained by centrifugation. The serum was sent to the blood test center of the First Affiliated Hospital of Jinan University. Then, all the nude mice were executed, and three nude mice were randomly selected from each group to have their tumors removed and fixed for pathological examination. Pathological examination indicators include H&E staining

and immunohistological examination. Immunohistological examination indicators include: (1) Ki67 (antigen identified by monoclonal antibody, cell proliferation index), (2) CD31 (platelet endothelial cell adhesion molecule-1, PECAM-1/CD31), (3) VEGF (vascular endothelial growth factor), and (4) TUNEL (TdT-mediated dUTP nick-end labeling, *in situ* end transferase labeling technology) expression levels.

2.17. Statistical analysis

Statistical analysis was performed using SPSS 18.0 statistical software, and all experiments were carried out at least in triplicate. The data were expressed as mean \pm standard deviation. The differences between the control and experimental groups were analyzed using a two-tailed Student's *t*-test. One-way analysis of variance (ANOVA) was used in multiple group comparisons. Differences with $p < .05$ (*) or $p < .01$ (**) are indicated.

3. Results and discussion

3.1. Rational design and characterization of F/A-PLGA@DOX/SPIO NPs

F/A-PLGA@DOX/SPIO NPs were successfully prepared and characterized by TEM, Zetasizer particle sizing, and FT-IR. Figure 1(a) and Figure S1 have shown the appearance of F/A-PLGA@DOX/SPIO. According to the Nano-ZS particle analyzer (Malvern Instruments Limited, Malvern, UK), the particle diameter and zeta electric potential of PLGA were 85 nm ($PDI = 0.261 \pm 0.006$) and -19.0 mV , respectively. DOX and SPIO were wrapped in PLGA through solvent evaporation method, then on its surface modified CS and targeting molecules FA and ACPP. After that, its particle diameter was 260 nm ($PDI = 0.254 \pm 0.017$) and zeta electric potential was $+28.7 \text{ mV}$ (Figure 1(b,c)). FT-IR (Equinox 55, Bruker, Billerica, MA, USA) was used to test the chemical construction and coupled type of the F/A-PLGA@DOX/SPIO. From the results in Figure 1(d) and Figure S3, in the spectrum of the oleic acid-modified SPIO, the peak at 1453.8 cm^{-1} was assigned to $-\text{CH}=\text{CH}-$ in the oleic acid. In the spectrum of CS-PLGA@DOX/SPIO, the $-\text{CH}=\text{CH}-$ peak was red-shifted to 1464.9 cm^{-1} . The peak at 1101.9 cm^{-1} in the spectrum of CS-PLGA@DOX/SPIO was assigned to $-\text{C}-\text{O}-\text{C}$ from the PLGA. The peaks at 1293.7 cm^{-1} and 1735.5 cm^{-1} were assigned to $=\text{C}-\text{O}-\text{C}$ and the fused aromatic ring from DOX, respectively. In the spectrum of CS-FA, the peak at 1561.6 cm^{-1} belonged to the primary amino groups of CS. The peaks at 1701.1 cm^{-1} belonged to the carboxylic groups from FA. The peak appeared at 1648.7 cm^{-1} was assigned to the newly formed amino groups between CS and FA. In the spectrum of CS-ACPP, the amide groups from ACPP and the new amide groups generated between CS and ACPP appeared at 1543.1 cm^{-1} and 1654.9 cm^{-1} . In the spectrum of F/A-PLGA@DOX/SPIO, the peaks at 1553.4 cm^{-1} and 1652.0 cm^{-1} were assigned to the amide groups from CS-FA and CS-ACPP. The peak at 1105.6 cm^{-1} was assigned to the $-\text{C}-\text{O}-\text{C}$ from PLGA. The peak at 1735.5 cm^{-1} was assigned to the $=\text{C}-\text{O}-\text{C}$

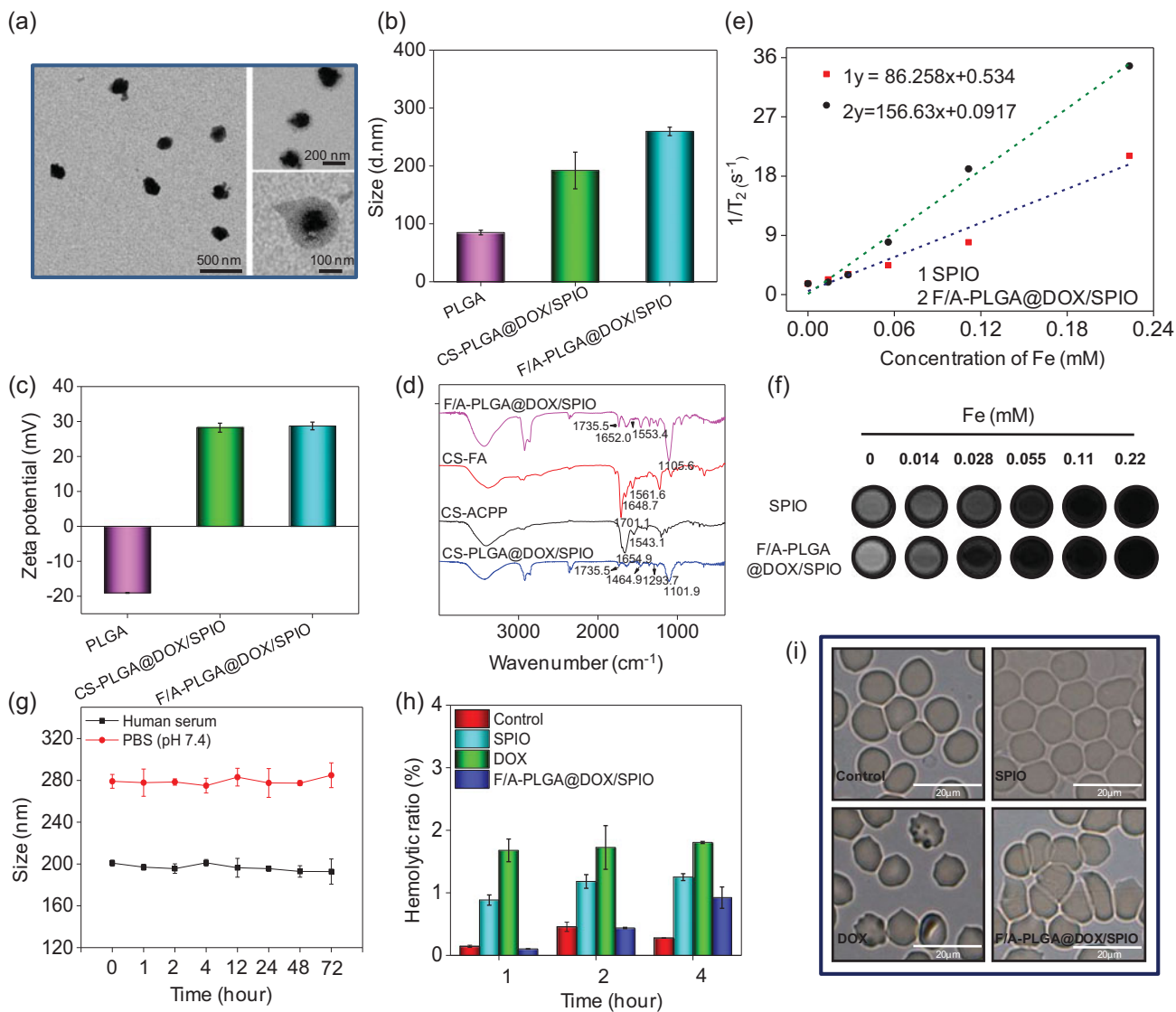


Figure 1. Characterization of F/A-PLGA@DOX/SPIO NPs. (a) TEM image of F/A-PLGA@DOX/SPIO NPs. (b) Size distribution of PLGA, CS-PLGA@DOX/SPIO, and F/A-PLGA@DOX/SPIO NPs. (c) Zeta potential of PLGA, CS-PLGA@DOX/SPIO, and F/A-PLGA@DOX/SPIO NPs. (d) FT-IR spectra of F/A-PLGA@DOX/SPIO, CS-FA, CS-ACPP, and CS-PLGA@DOX/SPIO NPs. (e) T2 relaxation rate (r_2) of SPIO and F/A-PLGA@DOX/SPIO NPs. (f) The concentration-dependent T2-weighted MR images of SPIO and F/A-PLGA@DOX/SPIO NPs. (g) Change in particle size of SPIO, DOX, and F/A-PLGA@DOX/SPIO NPs after incubation with human erythrocytes for 1, 2, and 4 h, in PBS and human serum. (h) Percentage of hemolysis caused by SPIO, DOX, and F/A-PLGA@DOX/SPIO NPs after 4-h incubation with human erythrocytes for 1, 2, and 4 h, respectively. (i) Human erythrocyte agglutination investigated by phase microscopy after 4-h incubation with SPIO, DOX, and F/A-PLGA@DOX/SPIO NPs, respectively. Values expressed as means \pm SD of triplicate.

from DOX. These results commonly demonstrated the structure of as-prepared F/A-PLGA@DOX/SPIO. As shown in Figure S4, chemical shifts of δ 7.65 and 6.94 represent hydrogen from 17/19 and 16/20 of low-field benzene ring, respectively; δ 8.66 represents hydrogen in the 8-bit carbon of the pteridine ring, suggestive of the successful linkage with FA. Meanwhile, PLGA was well connected in accordance with chemical shifts of δ 0.86 ($-\text{CH}_3$) and 1.24/1.48 ($-\text{CH}_2-$). CS was connected in accordance with chemical shifts of δ 3.60/3.66 representing hydrogen in a pyran ring and δ 4.11 ($-\text{OH}$). δ 3.93 and 3.42 ($-\text{CO}-\text{CH}_2-$) were methylene hydrogen linked to the carbonyl on ACPP, which showed that ACPP was successfully connected. To sum up, the results of the $^1\text{H-NMR}$ proved that F/A-CS-PLGA can be successfully prepared. The synthesized map of F/A-CS-PLGA can be seen in Figure S5. Taken together, these results suggest that F/A-PLGA@DOX/

SPIO NPs has been successfully synthesized for future biological and medicinal applications.

The transverse relaxation rate (r^2) is often used to measure the contrast radiography performance of MRIs. As shown in Figure 1(e,f), the dispersion of F/A-PLGA@DOX/SPIO at different concentrations was determined. It turned out that the transverse relaxation time ($1/T_2$) of F/A-PLGA@DOX/SPIO increased linearly with Fe concentration. The transverse relaxation rate (r^2) of SPIO was $86.258 \text{ mM}^{-1}\text{s}^{-1}$ while that of F/A-PLGA@DOX/SPIO was $156.63 \text{ mM}^{-1}\text{s}^{-1}$; performance of F/A-PLGA@DOX/SPIO was higher than commercialized SPIO (Wang et al., 2011; Li et al., 2015). The results indicate that F/A-PLGA@DOX/SPIO significantly improved relaxation performance, probably due to a large amount of SPIO tightly wrapped in the center of the nanosystem. Studies have shown that the relaxation rate of magnetic NPs is influenced

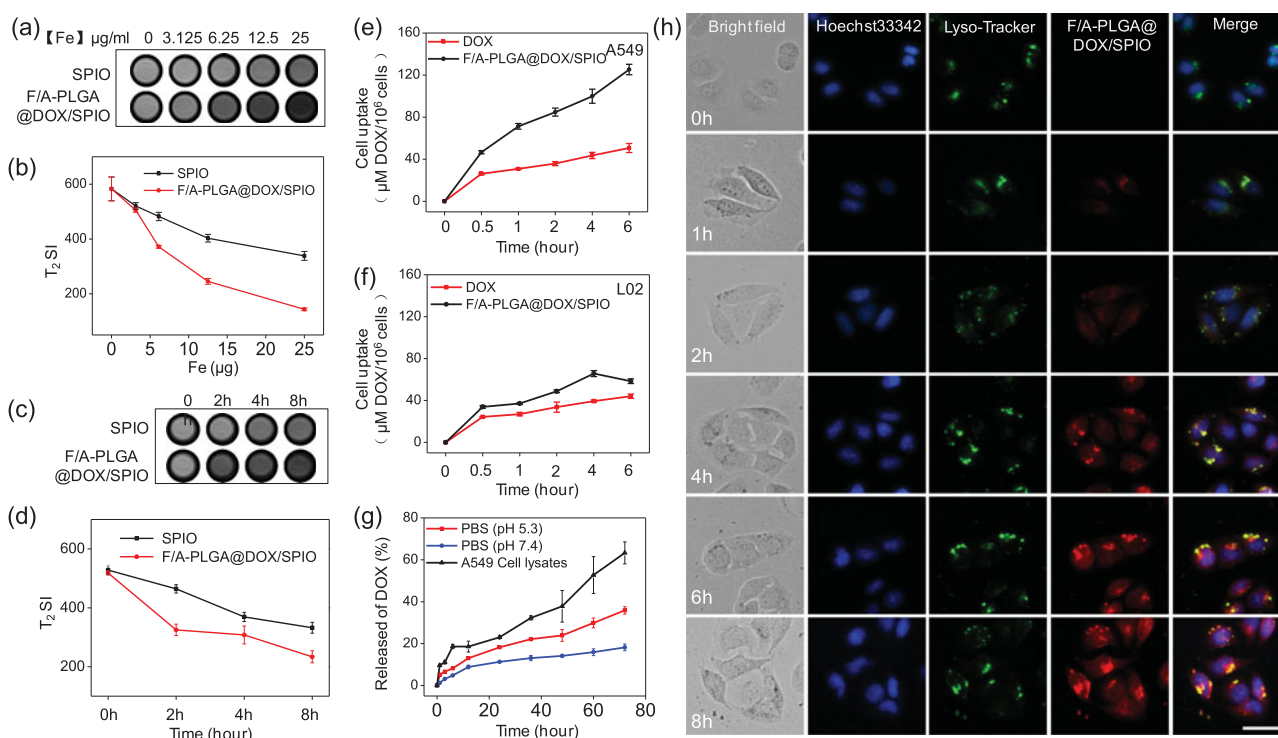


Figure 2. Selective cellular uptake and drug release of F/A-PLGA@DOX/SPIO NPs. T₂-weighted imaging (a) and iron uptake curves (b) of the A549 cells after incubation for 24 h with SPIO and F/A-PLGA@DOX/SPIO NPs at different Fe concentrations. T₂-weighted imaging (c) and iron uptake curves (d) of the A549 cells after incubation for 0, 2, 4, and 8 h with SPIO and F/A-PLGA@DOX/SPIO NPs at the same Fe concentration. Quantitative analysis of cellular uptake of DOX and F/A-PLGA@DOX/SPIO NPs in A549 (e) and L02 (f) cells. (g) In vitro release profiles of DOX from F/A-PLGA@DOX/SPIO in PBS solution at pH 5.3, pH 7.4, and A549 cell lysates, respectively. (h) Intracellular trafficking of F/A-PLGA@DOX/SPIO in A549 cells. A549 cells stained with Lyso-tracker (lysosome) and DAPI (nucleus) were treated with F/A-PLGA@DOX/SPIO for different periods of time. Values expressed as means \pm SD of triplicate.

by the macromolecule polymer layer wrapped around the surface (Kim et al., 2009; Tong et al., 2010). Higher r^2 causes a remarkable increase in the relaxation rate of water protons of F/A-PLGA@DOX/SPIO, which has great potential of being a MRI T₂ contrast medium.

3.2. Stability and hemocompatibility of NPs

The biological stability of the nanosystem is an important parameter to see whether it can be applied in human clinical trials (Service, 2003). A Nano-ZS particle analyzer (Malvern Instruments Limited, Malvern, UK) was used to test plasma stability of the F/A-PLGA@DOX/SPIO nanosystem. As shown in Figure 1(g), after incubation in human serum and PBS (pH 7.4) for 72 h, there is no significant change in the particle size of F/A-PLGA@DOX/SPIO. The F/A-PLGA@DOX/SPIO nanosystem is relatively stable, which can ensure more medicine is targeted at tumor tissue, providing support for its future applications in clinical trials and the medical field (Zeng et al., 2015).

The hemolytic rates of SPIO, DOX, and F/A-PLGA@DOX/SPIO were separately tested to assess their hemocompatibility. As illustrated in Figure 1(h), after 1-, 2-, and 4-h incubation with red blood cells, no obvious hemolysis (the rates are less than 5%) had been found on SPIO, DOX, or F/A-PLGA@DOX/SPIO; the hemolytic rate of F/A-PLGA@DOX/SPIO was less than 1%. As shown in Figure 1(i) and Figure S6, there was no significant change in the morphology of red blood cells in SPIO and F/A-PLGA@DOX/SPIO treatment

groups, but a little damage in DOX treatment group. These results indicated that no obvious hemolytic toxicity occurred in the F/A-PLGA@DOX/SPIO nanosystem.

3.3. In vitro magnetic resonance imaging of NPs

In vitro cell MRI was used to study the imaging effect of tumor cells after ingesting nanophase drugs. As shown in Figure 2(a,b), as the iron concentration increased, T₂-weighted signals for both contrast agents gradually decreased. Compared to SPIO of the same concentration, the T₂WI signal of F/A-PLGA@DOX/SPIO declined more distinctly. The results showed that the F/A-PLGA@DOX/SPIO nanosystem has strong targeting binding to A549 cells and could mediate the entry of more NPs into A549 cells. SPIO and F/A-PLGA@DOX/SPIO at the same concentration were scanned at different times through the T₂WI (Li et al., 2013; Li et al., 2015). As shown in Figure 2(c,d), T₂WI signal of the two contrast media gradually decreased over time and T₂WI signal reduction of the F/A-PLGA@DOX/SPIO nanosystem was more pronounced. These experiments demonstrated that F/A-PLGA@DOX/SPIO can be an excellent MRI T₂-negative contrast agent.

3.4. Selective cellular uptake and intracellular trafficking of NPs

The cellular uptake efficiency of drugs is one of the most crucial elements of anticancer activity. As shown in Figure

2(e), cellular uptake of F/A-PLGA@DOX/SPIO and DOX in A549 cells accumulates over time. Compared to DOX, the absorptivity of F/A-PLGA@DOX/SPIO in A549 cells increased significantly over time. Nevertheless, the accumulation of F/A-PLGA@DOX/SPIO and DOX in L02 cells was also time dependent and its absorptivity increases slightly (Figure 2(f)), though much less than its accumulation in A549 cells. This means that the F/A-PLGA@DOX/SPIO nanosystem improved the selectivity between normal cells and cancer cells.

Moreover, we explored the intracellular translocation of F/A-PLGA@DOX/SPIO in living cells. F/A-PLGA@DOX/SPIO has an advantage of location with green fluorescence when using a fluorescence microscope to carry out real-time supervision (Kwon et al., 2014). Lyso-tracker (green) and Hoechst 33342 (blue) were used to label the lysosomes and nucleus, respectively. The transportation and absorption of F/A-PLGA@DOX/SPIO in A549 cells were monitored in real time. As shown in Figure 2(h), after 1 h of cell incubation by F/A-PLGA@DOX/SPIO, a faint red fluorescent signal appeared in lysosomes. After 2 h, more green and red fluorescent signals overlapped in the lysosomes of A549 cells, which proved that many NPs entered the cells and settled in the lysosomes. After 4 h, the red signals in the lysosomes became stronger, and after 6 h, the red fluorescent signals expanded throughout the cytoplasm. These results suggest that F/A-PLGA@DOX/SPIO is mainly located in the lysosomes after entry the cell.

3.5. In vitro NPs drug release behavior

The therapeutic effect of drugs is also dependent on drug release efficiency, so we evaluated the drug release efficiency of NPs. Diverse solutions are used to simulate what NPs encounter *in vivo*. PBS (pH = 5.3), PBS (pH = 7.4), and A549 cell lysates were put in an imitated interior medium consisting of lysosomes, a hemato-microenvironment, and an intracellular environment to test the release rate of DOX in different media. As shown in Figure 2(g), the release profile of F/A-PLGA@DOX/SPIO in PBS solution (pH = 7.4) was modest and the release efficiency was only 18.2% after 72 h, indicating that F/A-PLGA@DOX/SPIO is more stable in internal blood circulation. However, the release efficiency of F/A-PLGA@DOX/SPIO in cell lysates of PBS (pH = 5.3) and A549 cells increased significantly to 35.7% and 63.3%, respectively. These results suggest that F/A-PLGA@DOX/SPIO can decompose in low pH, so that the DOX in the NPs can be released. Moreover, A549 cell lysates not only provide an acidic environment, but also contain hydrolytic enzymes, so it may be more capable of simulating the cellular lysosome environment, and the release of DOX is more efficient. Taken together, these data indicate that when F/A-PLGA@DOX/SPIO is absorbed by the cells and DOX is released under the action of lysosomes, an anticancer effect is exerted.

3.6. In vitro antitumor activity of F/A-PLGA@DOX/SPIO NPs and its mechanism

To evaluate the antitumor activity of the F/A-PLGA@DOX/SPIO nanosystem, MTT was used to detect the inhibiting

effects of DOX, FA-PLGA@DOX/SPIO, ACPP-PLGA@DOX/SPIO, and F/A-PLGA@DOX/SPIO on A549 and L02 cells. As in Figure 3(a), DOX produces inhibiting effects on A549 cells ($IC_{50} = 0.132 \mu\text{M}$), but also had a toxic effect on L02 cells ($IC_{50} = 0.097 \mu\text{M}$). After being modified by FA and ACPP, F/A-PLGA@DOX/SPIO exhibited a better anticancer effect and lower toxic than DOX. F/A-PLGA@DOX/SPIO produced significant higher antitumor activity in A549 cells, which were about 1.9 times higher than DOX. By comparison, the toxicity of L02 cells decreased using F/A-PLGA@DOX/SPIO ($IC_{50} = 0.207$) was 2.1 times lower than that of DOX ($IC_{50} = 0.097$). The SI of DOX was 0.73 while for F/A-PLGA@DOX/SPIO was 3.00, with its toxicity much lower than DOX.

As in Figure 3(b,c), F/A-PLGA@DOX/SPIO had a dosage-dependent growth inhibition of A549 and L02 cells in this experiment. Specifically, F/A-PLGA@DOX/SPIO increased the toxicity of DOX to A549 cells. It is noteworthy that F/A-PLGA@DOX/SPIO significantly reduced the toxicity of DOX to L02 cells. At the same time, the IC_{50} of F/A-PLGA@DOX/SPIO to L02 cells was much larger than A549 cells, which meant that the F/A-PLGA@DOX/SPIO nanosystem improved the selectivity of medicine between normal cells and tumor cells. This may be because FA can specifically recognize FR- α , which is overexpressed on the surface of malignant tumor cells (Campbell et al., 1991; Franklin et al., 1994). ACPP is a polypeptide with a response to tumor microenvironments and specialty in recognizing matrix metalloproteinases MMP-2/MMP-9 in various malignant tumor cells (Xia et al., 2013) for cell penetration. These results indicate that targeting decoration improves the absorption efficiency of cancer cells and makes F/A-PLGA@DOX/SPIO selective between normal cells and cancer cells.

In this study, we successfully prepared FR functionalized F/A-PLGA@DOX/SPIO to specifically recognize FR- α with overexpression on the surface of A549 cells, thereby increasing the active targeting of nanocarriers. For further validation, we examined the expression level of the FA receptors in A549, HeLa, A375, and L02 cells using Western blotting. As shown in Figure S7, FR- α in the membrane sheet of A549 cells had a higher expression that was conducive to the active targeting of F/A-PLGA@DOX/SPIO to A549 cells.

3.7. Induction of cell apoptosis by F/A-PLGA@DOX/SPIO NPs

Antitumor drugs generally inhibit cancer cell proliferation by inducing apoptosis and cycle arrest, eventually leading to tumor cell death (Huang et al., 2013). As shown in Figure 3(d), after treated with DOX, FA-PLGA@DOX/SPIO, ACPP-PLGA@DOX/SPIO, and F/A-PLGA@DOX/SPIO, the sub-G1 phase A549 cells increased from 2.7% to 7.8%, 10.7%, 20.1%, and 24.3%, respectively. These results showed that F/A-PLGA@DOX/SPIO may inhibit cell proliferation by inducing apoptosis. Compared to non-targeted or single-targeted NPs, dual-targeted NPs better promoted apoptosis. This may be because FA and ACPP dual-modified NPs can more easily

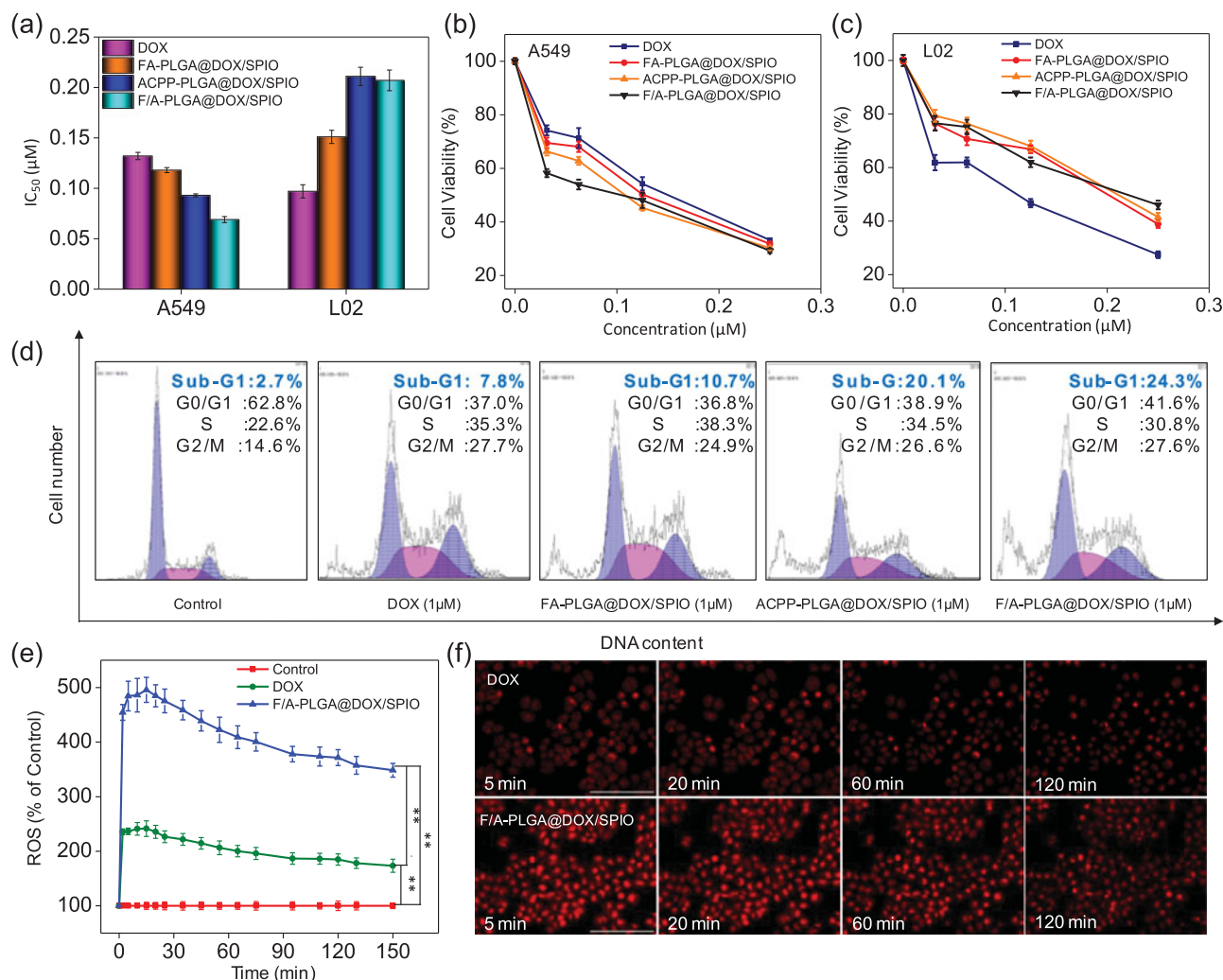


Figure 3. Induction of cell apoptosis by F/A-PLGA@DOX/SPIO NPs. (a) Proliferative inhibition of F/A-PLGA@DOX/SPIO against A549 and L02 cells for 72 h. A549 cells (b) and L02 cells (c) were treated with different concentrations of DOX, FA-PLGA@DOX/SPIO, ACPP-PLGA@DOX/SPIO, and F/A-PLGA@DOX/SPIO for 72 h. The cell viabilities were examined by MTT assay. (d) Flow cytometric analysis of A549 cell cycle distribution. (e) Overproduction of ROS in A549 cells detected by DHE fluorescence intensity. (f) Changes of ROS level in A549 cells incubated with DOX or F/A-PLGA@DOX/SPIO NPs for different periods of time. Values expressed as means \pm SD of triplicate. * $p < .05$ vs. control. ** $p < .01$ vs. control.

pass through the cell membrane to enhance anticancer activity and induce cell apoptosis.

Numerous studies have shown that overaccumulation of reactive oxygen species (ROS) leads to denaturation of cellular proteins or DNA damage through activation of p53 involved in the induction of apoptotic signaling by many anticancer chemotherapeutics (Pelicano et al., 2004; He et al., 2015; Li et al., 2016b; Zanganeh et al., 2016). ROS is a by-product of normal cellular aerobic metabolism, mainly including hydrogen peroxide (H_2O_2), superoxide (O_2^-), hydroxyl radical ($\cdot OH$), and singlet oxygen (1O_2). As shown in Figure 3(e,f), A549 cells showed various degrees of intracellular ROS increase regulation after being treated with F/A-PLGA@DOX/SPIO and DOX. F/A-PLGA@DOX/SPIO and DOX could significantly induce the production of ROS in A549 cells and maintain production at an elevated level following the increase to its maximum in 15 min. However, compared with F/A-PLGA@DOX/SPIO, DOX with the same concentration caused significantly lower amount of intracellular ROS production. Related studies have shown that doxorubicin-

induced apoptosis is more likely caused by excessive intracellular accumulation of ROS (Wang et al., 2004; Olson et al., 2010; Huang et al., 2013). It was suggested that F/A-PLGA@DOX/SPIO can induce apoptosis by promoting the overproduction of ROS in A549 cells.

3.8. In vivo MR R_2^* imaging of A549 tumor-bearing mice

As shown in Figure S8, the conventional T_2WI signals for the three groups of nude mice with subcutaneous tumors were relatively uniform. The tumors were mainly composed of parenchyma components with no obvious cystic necrosis. At present, the application of the MR R_2^* imaging sequence, which is a reliable and noninvasive tool to evaluate the iron content in living tissues, can sensitively detect changes of magnetic environment caused by the change of iron content in the body. It has been confirmed that there is a high correlation between iron content in the tissue and R_2^* value (Wood et al., 2005; Idilman et al., 2016; Li et al., 2016c). As

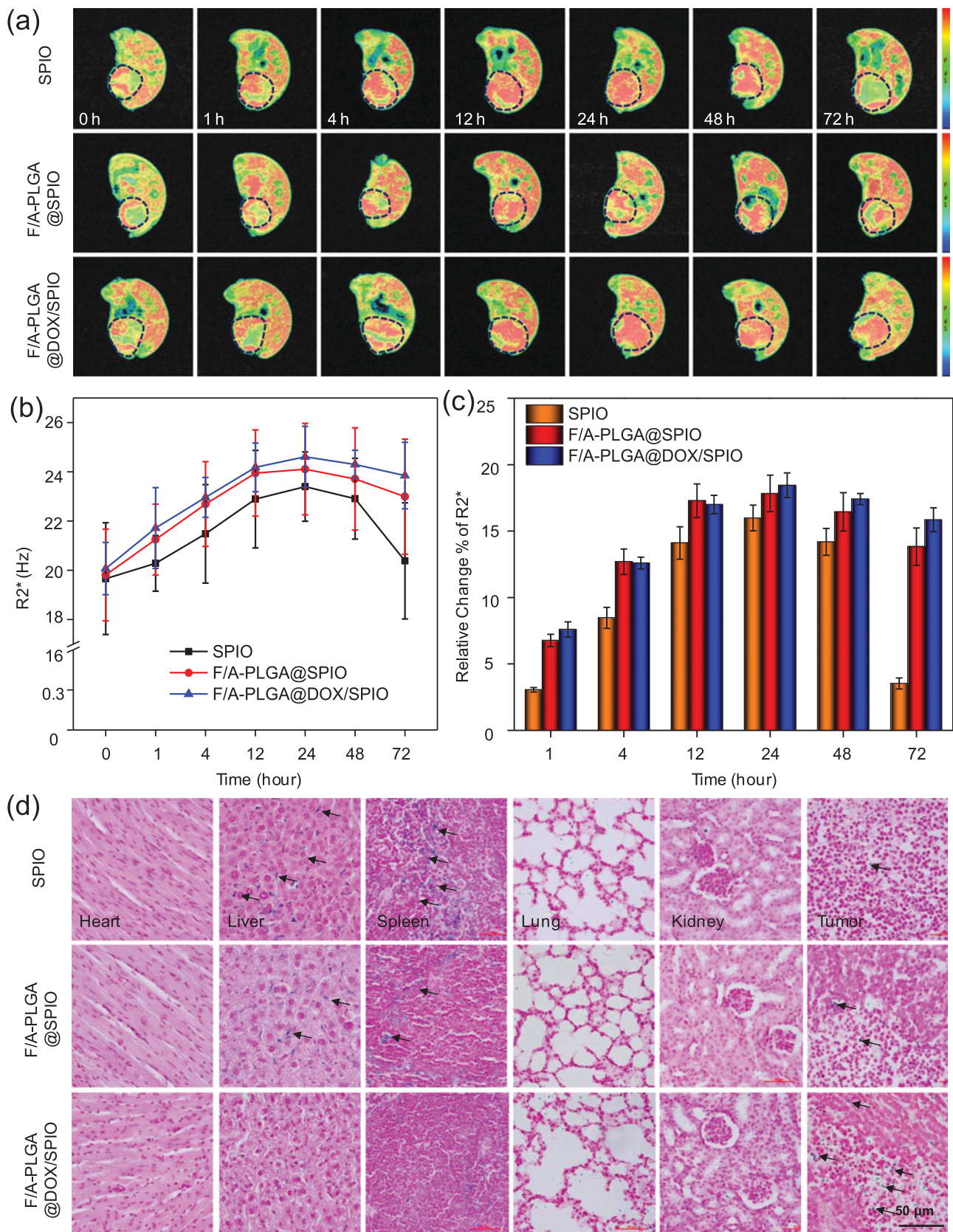


Figure 4. MR R_2^* imaging of A549-bearing mice after injecting contrast agents. (a) MR R_2^* maps of A549-bearing mice after injecting SPIO, F/A-PLGA@SPIO, and F/A-PLGA@DOX/SPIO NPs at different times. (b) Broken line chart of the changing trend of tumor R_2^* value for each group at different times. (c) Percentage of relative change of tumor R_2^* value for each group at different times. The tumor sites are circled by dashed lines. Values expressed as means \pm SD of triplicate. (d) Prussian blue staining analysis of the major organs collected from different treatments of A549-bearing mice after 72 h. Tumor, heart, liver, lung, spleen, and kidney (original magnification: 40 \times).

shown in Figure 4(a), the larger the orange-red region of the tumor becomes, the higher the R_2^* value of the tumor tissue will be. In Figure 4(b), compared to SPIO, the R_2^* value of tumors of the F/A-PLGA@SPIO and F/A-PLGA@DOX/SPIO NPs groups increased significantly at 1 h and 4 h, with R_2^* value decreasing slower at 48 h and 72 h than for the SPIO group. The R_2^* value of the tumors in the F/A-PLGA@SPIO NPs group peaked at 12 h and 24 h, and the R_2^* value in the F/A-PLGA@DOX/SPIO NPs group peaked at 24 h; both were higher than the SPIO group. Results for F/A-PLGA@DOX/SPIO pharmacokinetics are shown in Figure S9 and Table S1. The nanosystem could significantly prolong the half-life ($t_{1/2\beta}$), plasma drug content (AUC_{0-48h}), and maximum plasma concentration (C_{max}) of the drug *in vivo* while reducing the *in vivo* clearance rate (Cl), indicating that F/A-PLGA@DOX/SPIO has a relatively high plasma circulation time. According to Kuhlper et al. (2007), lung cancer cells were treated with two contrast agents, pure SPIO and receptor targeting marker SPIO; the latter had a higher R_2^* value. Pure SPIO was retested by the reticuloendothelial system, with the majority accumulated in the liver and spleen, while NPs with targeting structure were left in the tumor for a longer time. The surface functional modification of FA and ACPP can improve the active recognition of NPs and is more conducive to drug absorption in tumors. As shown in Figure 4(c), the R_2^* values of the F/A-PLGA@SPIO and F/A-PLGA@DOX/SPIO NPs group at each time relatively were higher than SPIO group. The total range increase of R_2^* value of the pure SPIO group for each scan was lower than that of the targeted contrast agent group and its excretory phase was significantly earlier than that of the targeted contrast agent group.

As shown in Figure S10, the total trend of R_2^* tumor-to-muscle contrast ratio and the tumor R_2^* value of each groups is basically paralleled. The R_2^* tumor-to-muscle contrast ratio of the targeted contrast agent groups at each time was relatively higher than SPIO group. Meanwhile, the F/A-PLGA@DOX/SPIO group had a high R_2^* tumor-to-muscle contrast when compared with the SPIO group and there were statistically significant differences of R_2^* tumor-to-muscle contrast ratio between two groups.

3.9. Pathological Prussian blue staining analysis

Prussian blue staining, as shown in Figure 4(d), revealed that there were more blue dye particles in the tumor, liver, and spleen of the mice. The positive staining rate of tumor tissue in the F/A-PLGA@SPIO and F/A-PLGA@DOX/SPIO NPs groups was significantly higher than in the SPIO group, while the positive staining rate in the liver and spleen tissues was significantly lower than in SPIO group. Prussian blue staining was used to carry out a qualitative analysis on the nanosystem in the nude mice tumors and the distribution of iron in various tissues and organs to further verify the results of the MR R_2^* imaging.

3.10. *In vivo* therapeutic effects of F/A-PLGA@DOX/SPIO

Body weight-time curves of nude mice in each group are shown in Figure 5(a). DOX (2 mg/kg) group showed a significant decrease in body weight 10 days after administration, with an average body weight of 17.02 g after 28 days which were significantly lower than the other groups. *In vivo* tumor growth-time curves are shown in Figure 5(b). After 28 days of administration, the tumor volume of the F/A-PLGA@DOX/SPIO (1 mg/kg) and F/A-PLGA@DOX/SPIO (2 mg/kg) groups was significantly smaller than that of the DOX (2 mg/kg) group. Tumor growth inhibition rate is shown in Figure 5(c) and the relative tumor growth rate is shown in Figure 5(d). Figure 5(e,f) shows the size and morphology of the nude mice as well as the size and shape of the dissected tumor. The tumor volume of the F/A-PLGA@DOX/SPIO (2 mg/kg) group was significantly smaller than that of other groups. The above results confirmed that the F/A-PLGA@DOX/SPIO nanosystem had better inhibitory effects on tumor growth than DOX.

H&E and immunohistochemistry analysis are shown in Figure 5(g). H&E staining showed that the tumor tissue of control group was relatively dense with obvious mitotic phases. Increased necrosis was observed in both F/A-PLGA@DOX/SPIO (1 mg/kg) and F/A-PLGA@DOX/SPIO (2 mg/kg) groups, especially for the latter. CD31 is commonly expressed in vascular endothelial cells and used to assess tumor angiogenesis (Piali et al., 1995). The CD31-positive staining rate of tumors in the F/A-PLGA@DOX/SPIO (2 mg/kg) group was significantly lower than the other groups. Ki67 can accurately reflect cell proliferation activity and has been widely used to determine the degree of malignancy of tumors (Lu et al., 2016). The Ki67-positive staining rate of tumors in the F/A-PLGA@DOX/SPIO (2 mg/kg) group was significantly lower than that of other groups. VEGF is secreted by various tumor cells and is the strongest and most specific angiogenic factor that induces tumor vascularization (Dvorak et al., 1995; Fan et al., 2008). The VEGF-positive staining rate of tumors in the F/A-PLGA@DOX/SPIO (2 mg/kg) group was significantly lower than that of other groups. DNA fragmentation is an important factor that leads to apoptosis and cell cycle arrest (Kilarkaje et al., 2014). In this study, TUNEL was used to determine whether F/A-PLGA@DOX/SPIO could induce tumor cell apoptosis. When tumor cells undergo apoptosis, nuclear pyknosis occurs, and nuclei are lysed into fragments of varied sizes to form apoptotic bodies. Cells are observed under a fluorescence microscope to show green fluorescence. As shown in Figure 5(g), almost no green fluorescence was observed in tumor cells of the control group after TUNEL staining. In the DOX (2 mg/kg) group, only a small amount of scattered green fluorescence can be seen in the tumor cells. Tumor cells in the F/A-PLGA@DOX/SPIO (1 mg/kg) and F/A-PLGA@DOX/SPIO (2 mg/kg) groups showed irregular distribution of green fluorescence, especially in the F/A-PLGA@DOX/SPIO (2 mg/kg) group. Overlapping TUNEL and DAPI staining images shows TUNEL-specific green fluorescence overlapped with blue fluorescence, resulting in a blue-green color. The above results

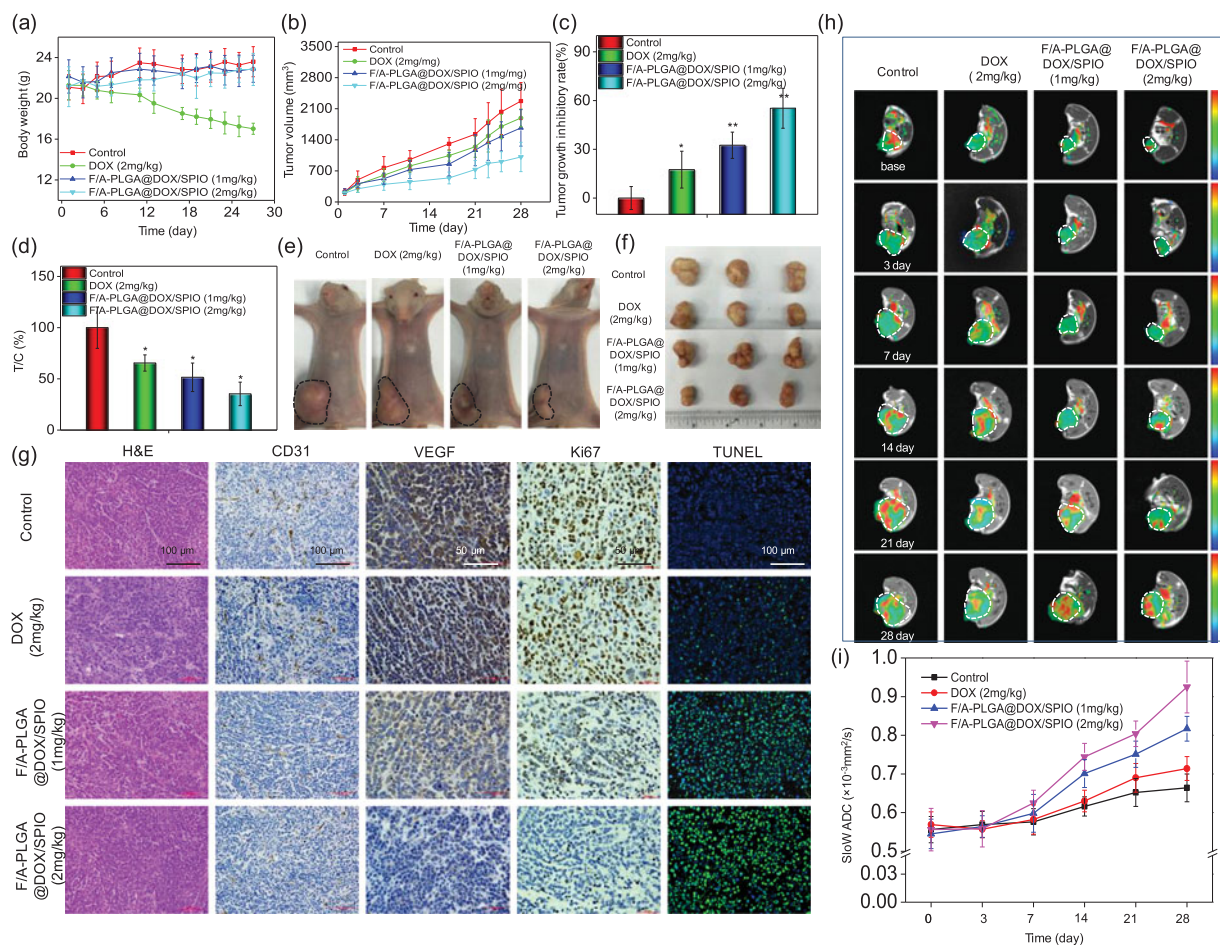


Figure 5. In vivo therapeutic effects of F/A-PLGA@DOX/SPIO NPs in A549-bearing mice. Body weight (a) and tumor volume (b) changes of A549 tumor-bearing mice following different treatments. The tumor growth inhibitory rate (c) and relative tumor proliferation rate (d) of different groups of A549 tumor-bearing mice at 28 days. Photographs of size and morphology of tumors (e) and tumor gross specimens (f) from different groups of mice 28 days after the treatment (scale: 1 cm). Bars with different characteristics are statistically different at the $p < .05$ level. * $p < .05$ vs. control. ** $p < .01$ vs. control. (g) H&E, immunohistochemically analysis, and TUNEL staining in tumor sections from different treatment groups. Original magnification of H&E, CD31, and TUNEL: 20 \times ; original magnification of Ki67 and VEGF: 40 \times . (h) MR slow ADC maps of A549-bearing mice after different treatment groups at different times. Tumor sites are circled by dashed lines. (i) Broken line chart of the changing trend of tumor slow ADC value for each group at different times. Values expressed as means \pm SD ($n \geq 15$).

further verified that the F/A-PLGA@DOX/SPIO nanosystem has a better inhibitory effect on tumor growth than DOX.

3.11. Evaluation of therapeutic effects by IVIM-DWI MRI

The MRI can give precise and accurate positioning and quantitative analysis on lesions from the molecular level while demonstrating the anatomy of the tissue, which is suitable for dynamic detection and evaluation of efficacy. As shown in Figure S11, T₂WI had clear tumor boundaries with uniform signals within 7 days. The tumor was mainly composed of solid components. Seven days later, tumors showed various degrees of necrosis, hemorrhage, and steatosis with a visible, irregular high-low mixed signal area. In recent years, related studies have used quantitative parameters of IVIM-DWI, in which the slow ADC value represents pure water diffusion, to distinguish tumor necrosis from viable tissue by slow apparent diffusion coefficient (ADC) value and dynamically monitor changes caused by drug-induced cell density of tumors to make an early prediction for treatment method

and drug efficacy (Bozkurt et al., 2011; Joo et al., 2014; Cui et al., 2015; Joo et al., 2016; Lam et al., 2016).

As shown in Figure 5(h), the red area of the tumors in the F/A-PLGA@DOX/SPIO (1 mg/kg) and F/A-PLGA@DOX/SPIO (2 mg/kg) groups was relatively large, indicating that tumor cell density decreased with the enlargement of necrosis. In Figure 5(i), there was no significant increase in the slow ADC value of each group within 7 days. From day 7 to day 28, the slow ADC value of each group showed different degrees of upward trend. The slow ADC value of the control group showed a slow upward trend throughout the 28 days and was lower than that of the other groups, while the slow ADC value of the F/A-PLGA@DOX/SPIO (2 mg/kg) group increased most obviously. The slow ADC values of the DOX (2 mg/kg), F/A-PLGA@DOX/SPIO (1 mg/kg), and F/A-PLGA@DOX/SPIO (2 mg/kg) groups did not change significantly within 7 days, which was mainly due to cytotoxic edema. DOX caused tumor cells to be swollen and the diffusion of intracellular and extracellular water molecules was limited; however, the effect of DOX existed a time delay. From day 7 to day 28, with the delay of DOX treatment, tumor necrosis and

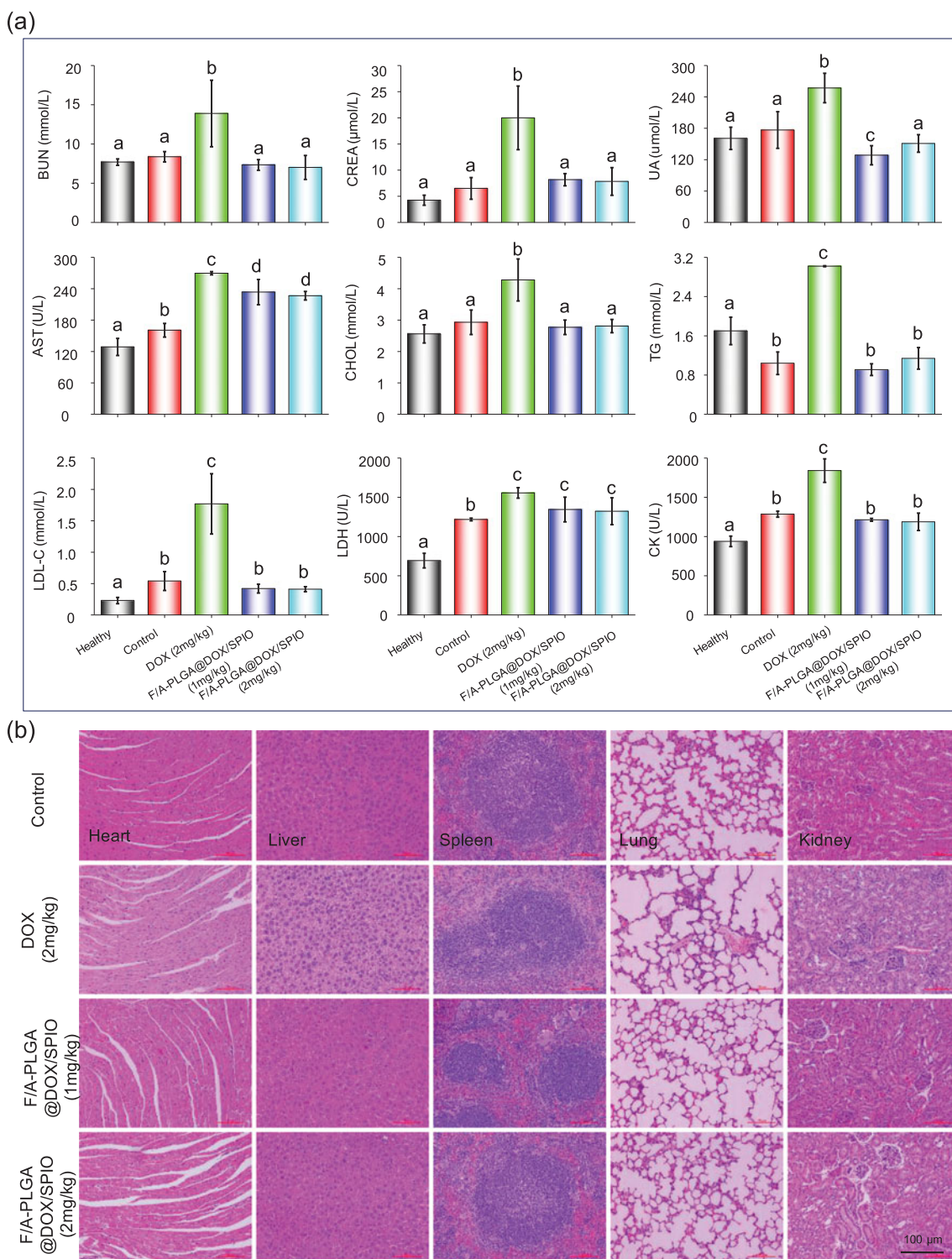


Figure 6. Toxicity assessment of F/A-PLGA@DOX/SPIO. (a) Hematological analysis of normal and different treatments of nude mice after 28 days. Serum biochemistry indexes including blood glucose (GLU), low-density lipoprotein cholesterol (LDL-C), total protein (TP), aspartate aminotransferase (AST), blood urea nitrogen (BUN), uric acid (UA), creatine kinase (CK), creatinine (CREA), serum total cholesterol (CHOL), triglyceride (TG), and lactate dehydrogenase (LDH). Values expressed as means ± SD of triplicate. Bars with different characters (a, b, c, and d) are statistically different at the $p < .05$ level. (b) Histology analysis of the major organs collected from different treatments of A549 tumor-bearing mice after 28 days (original magnification: 20×).

apoptosis gradually increased, and the degree of diffusion of water molecules was limited. The slow ADC value of each group slowly grew during this stage. According to a research by Chiaradia et al. (2014), as the extent of necrosis in the lesion of liver cancer increased, the slow ADC value also increased. Zhu et al. (2016) used IVIM-DWI to evaluate

chemotherapeutic effects in cervical cancer patients, with the slow ADC value gradually increasing throughout the chemotherapy cycle. These experimental results are consistent with the results of this study. In summary, through the slow ADC value of IVIM-DWI, one can dynamically monitor intracellular tumor cell density and necrosis range to detect and evaluate

the efficacy of the F/A-PLGA@DOX/SPIO nanosystem timely and accurately.

3.12. In vivo toxicity evaluation

To further assess the potential *in vivo* toxicity of F/A-PLGA@DOX/SPIO nanosystem, blood samples were drawn for hematology analysis after the experiment. The results, shown in Figure 6(a), indicated that tumor-bearing mice serum lipid indicators (low-density lipoprotein cholesterol (LDL-C), triglyceride (TG)), liver function indicator (aspartate aminotransferase (AST)), kidney function indicators (urea nitrogen (BUN), creatinine (CREA), uric acid (UA)), and cardiac function indicators (lactate dehydrogenase (LDH), creatine kinase (CK)) of the DOX (2 mg/kg) group were significantly higher than those of the control, F/A-PLGA@DOX/SPIO (1 mg/kg), and F/A-PLGA@DOX/SPIO (2 mg/kg) groups. The results show that DOX had toxic side effects and that the liver, kidney, and myocardial functions of tumor-bearing mice were severely impaired. F/A-PLGA@DOX/SPIO nanosystem significantly alleviated the damages of the functions of liver, kidney, and myocardium of tumor-bearing mice. Besides, as shown in Figure 6(b), the tumor tissues and histological sections of major organs of each group were stained with H&E, and there was blood in the alveoli of the DOX (2 mg/kg) group. The glomerular structure was destroyed as well. No obvious disease or inflammation was found in the main organs of the F/A-PLGA@DOX/SPIO (1 mg/kg) and F/A-PLGA@DOX/SPIO (2 mg/kg) groups. H&E staining and biochemical markers of the blood further illustrated DOX damage to multiple organs. However, the F/A-PLGA@DOX/SPIO nanosystem synthesized in this study did not show any obvious side effects such as organ damage, which decreased *in vivo* toxicity; thus, it is a relatively safe and multifunctional nanosystem *in vivo*.

4. Conclusions

Herein, the multifunctional F/A-PLGA@DOX/SPIO nanosystem has been rationally designed and found to exhibit good tumor targeting capability while reducing toxicity to normal tissues and organs. The F/A-PLGA@DOX/SPIO nanosystem can induce apoptosis by accelerating the overproduction of ROS in tumor cells. MR R_2^* imaging sequence is an imaging method of tracing and measuring intracellular SPIO in tumor cells for tumor-targeted imaging. In the nude mice model, F/A-PLGA@DOX/SPIO nanosystem has good biocompatibility and long plasma cycle time, making the release of DOX controllable and sustainable, which is conducive to the selective absorption of drugs within the tumor. The slow ADC value of IVIM-DWI showed that the range of tumor necrosis in the F/A-PLGA@DOX/SPIO group was larger than that of DOX alone. Meanwhile, according to hematological and histological analysis, no significant damage or inflammation was observed in major organs. In summary, F/A-PLGA@DOX/SPIO, a multifunctional nanosystem, has exciting potential to be an efficient and safe means for cancer treatment.

Disclosure statement

The authors declare no conflict of interest arising from this work.

Funding

This work was supported by National High-level Personnel of Special Support Program (W02070191), Natural Science Foundation of China (21701051), Natural Science Foundation of China (81771973), Science and Technology Planning Project of Guangdong Province, China (2017A020215065).

References

- Bozkurt M, Doganay S, Kantarci M, et al. (2011). Comparison of peritoneal tumor imaging using conventional MR imaging and diffusion-weighted MR imaging with different b values. *Eur J Radiol* 80:224–8.
- Campbell IG, Jones TA, Foulkes WD, Trowsdale J. (1991). Folate-binding protein is a marker for ovarian cancer. *Cancer Res* 51:5329–38.
- Chen T, Wong Y-S. (2009a). Selenocystine induces caspase-independent apoptosis in MCF-7 human breast carcinoma cells with involvement of p53 phosphorylation and reactive oxygen species generation. *Int J Biochem Cell Biol* 41:666–76.
- Chen T, Wong Y-S. (2009b). Selenocystine induces reactive oxygen species-mediated apoptosis in human cancer cells. *Biomed Pharmacother* 63:105–13.
- Chen X, Gambhir SS, Cheon J. (2011). Theranostic nanomedicine. *Acc Chem Res* 44:841.
- Chiaradia M, Baranes L, Van Nhieu JT, et al. (2014). Intravoxel incoherent motion (IVIM) MR imaging of colorectal liver metastases: are we only looking at tumor necrosis? *J Magn Reson Imaging* 39:317–25.
- Chu M, Shao Y, Peng J, et al. (2013). Near-infrared laser light mediated cancer therapy by photothermal effect of Fe₃O₄ magnetic nanoparticles. *Biomaterials* 34:4078–88.
- Cui Y, Zhang C, Li X, et al. (2015). Intravoxel incoherent motion diffusion-weighted magnetic resonance imaging for monitoring the early response to ZD6474 from nasopharyngeal carcinoma in nude mouse. *Sci Rep* 5:16389.
- Dvorak HF, Brown LF, Detmar M, Dvorak AM. (1995). Vascular permeability factor/vascular endothelial growth factor, microvascular hyperpermeability, and angiogenesis. *Am J Pathol* 146:1029–39.
- Fan C, Chen J, Wang Y, et al. (2013). Selenocystine potentiates cancer cell apoptosis induced by 5-fluorouracil by triggering reactive oxygen species-mediated DNA damage and inactivation of the ERK pathway. *Free Radic Biol Med* 65:305–16.
- Fan X, Krieg S, Kuo CJ, et al. (2008). VEGF blockade inhibits angiogenesis and reepithelialization of endometrium. *FASEB J* 22:3571–80.
- Fang C, Kievit FM, Veiseh O, et al. (2012). Fabrication of magnetic nanoparticles with controllable drug loading and release through a simple assembly approach. *J Control Release* 162:233–41.
- Franklin WA, Waintrub M, Edwards D, et al. (1994). New anti-lung-cancer antibody cluster 12 reacts with human folate receptors present on adenocarcinoma. *Int J Cancer* 57:89–95.
- He L, Lai H, Chen T. (2015). Dual-function nanosystem for synergetic cancer chemo-/radiotherapy through ROS-mediated signaling pathways. *Biomaterials* 51:30–42.
- Huang Y, He L, Liu W, et al. (2013). Selective cellular uptake and induction of apoptosis of cancer-targeted selenium nanoparticles. *Biomaterials* 34:7106–16.
- İdilman İS, Haliloğlu M, Gümruk F, Karçaaltıncaba M. (2016). The feasibility of magnetic resonance imaging for quantification of liver, pancreas, spleen, vertebral bone marrow, and renal cortex R_2^* and proton density fat fraction in transfusion-related iron overload. *TJH* 33:21–7.
- Jafari A, Salouti M, Shayesteh SF, et al. (2015). Synthesis and characterization of Bombesin-superparamagnetic iron oxide nanoparticles as a targeted contrast agent for imaging of breast cancer using MRI. *Nanotechnology* 26:075101.

- Joo I, Lee JM, Grimm R, et al. (2016). Monitoring vascular disrupting therapy in a rabbit liver tumor model: relationship between tumor perfusion parameters at IVIM diffusion-weighted MR imaging and those at dynamic contrast-enhanced MR imaging. *Radiology* 278:104–13.
- Joo I, Lee JM, Han JK, Choi BI. (2014). Intravoxel incoherent motion diffusion-weighted MR imaging for monitoring the therapeutic efficacy of the vascular disrupting agent CKD-516 in rabbit VX2 liver tumors. *Radiology* 272:417–26.
- Kilarkaje N, Al-Hussaini H, Al-Bader MM. (2014). Diabetes-induced DNA damage and apoptosis are associated with poly (ADP ribose) polymerase 1 inhibition in the rat testis. *Eur J Pharmacol* 737:29–40.
- Kim D-H, Zeng H, Ng TC, Brazel CS. (2009). T-1 and T-2 relaxivities of succimer-coated MFe₂₃+O₄ (M=Mn²⁺, Fe²⁺ and Co²⁺) inverse spinel ferrites for potential use as phase-contrast agents in medical MRI. *J Magn Magn Mater* 321:3899–904.
- Kim HS, Oh SY, Joo HJ, et al. (2010). The effects of clinically used MRI contrast agents on the biological properties of human mesenchymal stem cells. *NMR Biomed* 23:514–22.
- Kuhlpeter R, Dahnke H, Matuszewski L, et al. (2007). R2 and R2* mapping for sensing cell-bound superparamagnetic nanoparticles: *in vitro* and murine *in vivo* testing. *Radiology* 245:449–57.
- Kwon S, Singh RK, Kim T-H, et al. (2014). Luminescent mesoporous nanoreservoirs for the effective loading and intracellular delivery of therapeutic drugs. *Acta Biomater* 10:1431–42.
- Lam MK, Oerlemans C, Froeling M, et al. (2016). DCE-MRI and IVIM-MRI of rabbit Vx2 tumors treated with MR-HIFU-induced mild hyperthermia. *J Ther Ultrasound* 4:9.
- Li H, Yan K, Shang Y, et al. (2015). Folate-bovine serum albumin functionalized polymeric micelles loaded with superparamagnetic iron oxide nanoparticles for tumor targeting and magnetic resonance imaging. *Acta Biomater* 15:117–26.
- Li J, Zheng L, Cai H, et al. (2013). Polyethyleneimine-mediated synthesis of folic acid-targeted iron oxide nanoparticles for *in vivo* tumor MR imaging. *Biomaterials* 34:8382–92.
- Li L, Gao F, Jiang W, et al. (2016a). Folic acid-conjugated superparamagnetic iron oxide nanoparticles for tumor-targeting MR imaging. *Drug Deliv* 23:1726–33.
- Li Q, Liu C, Li H. (2016b). Induction of endogenous reactive oxygen species in mitochondria by fullerene-based photodynamic therapy. *J Nanosci Nanotechnol* 16:5592–7.
- Li W, Zhang Z, Gordon AC, et al. (2016c). SPIO-labeled yttrium microspheres for MR imaging quantification of transcatheter intrahepatic delivery in a rodent model. *Radiology* 278:405–12.
- Lu C, Xu H, Xu J, et al. (2016). Multi-pass adaptive voting for nuclei detection in histopathological images. *Sci Rep* 6:33985.
- Ma B, He L, You Y, et al. (2018). Controlled synthesis and size effects of multifunctional mesoporous silica nanosystem for precise cancer therapy. *Drug Deliv* 25:293–306.
- Maeng JH, Lee DH, Jung KH, et al. (2010). Multifunctional doxorubicin loaded superparamagnetic iron oxide nanoparticles for chemotherapy and magnetic resonance imaging in liver cancer. *Biomaterials* 31:4995–5006.
- Majd MH, Asgari D, Barar J, et al. (2013). Tamoxifen loaded folic acid armed PEGylated magnetic nanoparticles for targeted imaging and therapy of cancer. *Colloids Surf B Biointerfaces* 106:117–25.
- Rajendran JG, Mankoff DA. (2007). A definition of molecular imaging. *J Nucl Med* 48:855.
- Mcbain SC, Yiu HHP, Dobson J. (2008). Magnetic nanoparticles for gene and drug delivery. *Int J Nanomed* 3:169–80.
- Nazir S, Hussain T, Ayub A, et al. (2014). Nanomaterials in combating cancer: therapeutic applications and developments. *Nanomedicine* 10:19–34.
- Nogueira DR, Mitjans M, Infante MR, Vinardell MP. (2011). The role of counterions in the membrane-disruptive properties of pH-sensitive lysine-based surfactants. *Acta Biomater* 7:2846–56.
- Olson ES, Jiang T, Aguilera TA, et al. (2010). Activatable cell penetrating peptides linked to nanoparticles as dual probes for *in vivo* fluorescence and MR imaging of proteases. *Proc Natl Acad Sci USA* 107:4311–16.
- Pelicano H, Carney D, Huang P. (2004). ROS stress in cancer cells and therapeutic implications. *Drug Resist Updat* 7:97–110.
- Piali L, Hammel P, Uherek C, et al. (1995). CD31/PECAM-1 is a ligand for alpha v beta 3 integrin involved in adhesion of leukocytes to endothelium. *J Cell Biol* 130:451–60.
- Rossi A, Chiodini P, Sun J-M, et al. (2014). Six versus fewer planned cycles of first-line platinum-based chemotherapy for non-small-cell lung cancer: a systematic review and meta-analysis of individual patient data. *Lancet Oncol* 15:1254–62.
- Service RF. (2003). American Chemical Society meeting. Nanomaterials show signs of toxicity. *Science* 300:243.
- Sherry AD, Woods M. (2008). Chemical exchange saturation transfer contrast agents for magnetic resonance imaging. *Annu Rev Biomed Eng* 10:391–411.
- Tong S, Hou S, Zheng Z, et al. (2010). Coating optimization of superparamagnetic iron oxide nanoparticles for high T2 relaxivity. *Nano Lett* 10:4607–13.
- Veeravagu A, Liu Z, Niu G, et al. (2008). Integrin alpha(v)beta(3)-targeted radioimmunotherapy of glioblastoma multiforme. *Clin Cancer Res* 14:7330–9.
- Wang D-W, Zhu X-M, Lee S-F, et al. (2013). Folate-conjugated Fe₃O₄@SiO₂@gold nanorods@ mesoporous SiO₂ hybrid nanomaterial: a theranostic agent for magnetic resonance imaging and photothermal therapy. *J Mater Chem B* 1:2934–42.
- Wang LA, Neoh KG, Kang ET, Shuter B. (2011). Multifunctional polyglycerol-grafted Fe₃O₄@SiO₂ nanoparticles for targeting ovarian cancer cells. *Biomaterials* 32:2166–73.
- Wang SW, Konorev EA, Kotamraju S, et al. (2004). Doxorubicin induces apoptosis in normal and tumor cells via distinctly different mechanisms – intermediacy of H₂O₂- and p53-dependent pathways. *J Biol Chem* 279:25535–43.
- Wood JC, Enriquez C, Ghugre N, et al. (2005). MRI R2 and R2* mapping accurately estimates hepatic iron concentration in transfusion-dependent thalassemia and sickle cell disease patients. *Blood* 106:1460–5.
- Xia HM, Gu GZ, Hu QY, et al. (2013). Activatable cell penetrating peptide-conjugated nanoparticles with enhanced permeability for site-specific targeting delivery of anticancer drug. *Bioconjug Chem* 24:419–30.
- Yang X, Hong H, Grailer JJ, et al. (2011). cRGD-functionalized, DOX-conjugated, and Cu-64-labeled superparamagnetic iron oxide nanoparticles for targeted anticancer drug delivery and PET/MR imaging. *Biomaterials* 32:4151–60.
- Zanganeh S, Hutter G, Spitler R, et al. (2016). Iron oxide nanoparticles inhibit tumor growth by inducing pro-inflammatory macrophage polarization in tumor tissues. *Nature Nanotech* 11:986–94.
- Zeng L, Chen J, Ji S, et al. (2015). Construction of a cancer-targeted nanosystem as a payload of iron complexes to reverse cancer multidrug resistance. *J Mater Chem B* 3:4345–54.
- Zhu L, Zhu L, Shi H, et al. (2016). Evaluating early response of cervical cancer under concurrent chemo-radiotherapy by intravoxel incoherent motion MR imaging. *BMC Cancer* 16:79.